Selecting non-halogenated low-toxic hole transporting materials for Roll-to-Roll perovskite solar cells using carbon electrodes

Check for updates

Ershad Parvazian[1], David Beynon [1], Olivia Jenkins[1], Rahul Patidar[1], James Mcgettrick[1], Samual Ngombe[1], Bhushan Patil[1], Rodrigo Garcia-Rodriguez[1], Karen Valadez Villalobos[1], Peter Davies[2], Mathew Davies[1] & Trystan Watson [1] ✉

Perovskite solar cells hold promise for cost-effective, high-efficiency renewable energy generation; yet their commercialization is hindered by progress towards scalable fabrication methods. Roll-to-roll processing is a promising solution for large-scale production, and the incorporation of Roll-to-roll coated carbon electrodes offers several additional advantages, including low-cost manufacturing and high-stability. Introducing a compatible hole transporting layer between perovskite and carbon significantly improves performance. Here we present a study comparing four interlayers (Spiro-MeOTAD, PTAA, PEDOT, and P3HT) in printed devices, assessing efficiency, stability, and scalability. Our results reveal that spiro-MeOTAD and PTAA was not compatible with the carbon electrode however PEDOT and P3HT showed promising results. Beyond photovoltaic performance, comparison of P3HT and PEDOT in terms of stability, toxicity, and cost reveals that P3HT can be a superior choice for scaling up manufacturing. These findings offer valuable insights for optimizing perovskite solar cells performance in scalable production via roll-to-roll printing.

Perovskite solar cells (PSCs) offer a promising alternative to conventional silicon-based solar cells due to their high-power conversion efficiency (PCE) and cost-effectiveness[1–3]. They can be manufactured using simple techniques and are compatible with flexible substrates, making them suitable for large-scale commercialization and integration into emerging applications such as low light internet of things devices and building-integrated photovoltaics[4–9]. This development can play a key role in the shift towards sustainable and renewable energy sources.

Although PSCs have shown tremendous potential in laboratory-scale devices, their widespread commercialization has been hindered by the remaining challenges associated with their scalability, stability and production costs[10–13]. However, there have been promising reports on the successful scaling and enhanced stability of these devices recently.

In terms of the scale-up of PSCs, a diverse array of techniques has been investigated, each offering unique benefits and facing distinct challenges. These methods include solution-based[14,15] approaches such as slot-die, blade, and spray coatings, along with inkjet printing. Additionally,

evaporation techniques[16–18], notably thermal evaporation and flash infrared annealing, have been utilized. Furthermore, hybrid techniques[19,20] are emerging as a promising approach. These involve combining solution processing for specific layers, like the perovskite absorber, with vacuum processes, such as sputtering or evaporation, for creating contacts or buffer layers. While all these techniques play a crucial role and warrant serious research consideration, solution-based techniques stand out for certain practical advantages[16,20,21]. These advantages include cost-effectiveness, ease of coating, and a clearer path to commercialization when compared to evaporation and hybrid methods[22]. Unlike evaporation methods that require costly high-vacuum systems, solution-based approaches use simpler and more affordable equipment, significantly reducing production expenses. Additionally, these methods are inherently suited for large-scale production, particularly through roll-to-roll (R2R) processing, which is key for industrial scalability. In terms of operational simplicity, solution-based techniques offer easier optimization of film thickness and are more adaptable to a variety of substrates compared to the precision and complexity

[1]SPECIFIC IKC, Faculty of Science and Engineering, Swansea University, Fabian way, Swansea SA1 8EN, UK. [2]AIM, Faculty of Science and Engineering, Swansea University, Fabian way, Swansea SA1 8EN, UK. ✉e-mail: t.m.watson@swansea.ac.uk

required in vacuum-based evaporation and hybrid methods. This simplicity not only lessens production challenges but also speeds up the transition from lab-scale research to commercial products.

To achieve solution-based scalability, the R2R coating techniques, including spray, gravure, knife/blade, and slot-die coating, have emerged as a promising approach[23–28]. These techniques enable high-throughput deposition of the solution-based materials onto flexible substrates in a continuous manner, facilitating efficient, reproducible, and low-cost production of PSCs on a large scale. While each of these techniques plays a role in the production of inline perovskite photovoltaics, most are not versatile enough to be used for inline full-device coatings. For example, while spray coating leads to highly efficient perovskite devices[29–31], it introduces environmental and health risks in large-area R2R manufacturing due to the spread and aerosolization of solvents, particularly those that are highly toxic. This factor restricts its use in applying the perovskite layer, particularly in open spaces[32]. Additionally, this technique tends to consume significantly more solution compared to other R2R coating methods[33]. In contrast, R2R blade coating and slot-die (SD) coating methods present fewer environmental concerns due to significantly lower solution consumption and greater control over the coating area[34–36]. Blade coating offers benefits, including the ability to use a wide range of fluids, encompassing both high and low viscosities[37]. In addition, blade coating is more advantageous at the lab scale compared to slot-die coating, as it avoids issues with dead volume encountered in the latter. This results in reduced ink consumption for small batch processing[38,39]. However, compared to slot-die, blade coating can have challenges in achieving uniformity in the deposited layers, due to reduced control of the coating parameters, especially over large areas. Slot-die coating typically offers faster coating speeds than spray coating and inkjet printing. Additionally, it allows for more precise control of layer thickness and uniformity compared to spray coating, blade coating, and gravure coating. These advantages make slot-die coating a superior choice among roll-to-roll compatible coating methods[40,41]. Previous studies have successfully employed the R2R slot-die coating method to deposit all the layers, except for the top electrode, which is typically made of a precious and rare metal (gold or silver) which is deposited through thermal evaporation, making it incompatible with ambient roll-to-roll processing[32,42–47].

Carbon electrodes have garnered considerable attention as a viable option for employment in PSCs, owing not only to their hydrophobic characteristics and high thickness, which enhance the stability of the cells, but also to their compatibility with the coating processes associated with roll-to-roll manufacturing[48–50]. Additionally, carbon electrodes offer further advantages such as cost-effectiveness, high flexibility, and the ability to achieve PCEs that are comparable to those achieved with conventional metal electrodes[51,52].

Despite the advantages offered by carbon electrodes, they still present certain challenges, particularly in terms of weak charge transfer when directly coated on top of the perovskite layer, owing to poor interface contact and high energy level difference between perovskite and carbon[53–55]. Additionally, the compatibility of the solvent system used with the underlying layers poses a significant hindrance when coating carbon on conventional hole-transporting interlayers. To address both issues, various studies have suggested methods to tailor the energy level alignment, such as implementing appropriate surface treatments, using compatible interlayers, or adding proper dopants to the solution before coating, to improve the charge transfer from perovskite to carbon[55–59]. Notably, a recent study in using carbon ink as a solution-based material have enabled successful R2R printing of all layers in PSCs, including the top electrode, representing a significant milestone in implementing this technology[60]. However, this work focussed exclusively on PEDOT without considering the wider opportunities for alternative materials.

In this study, we introduce a facile approach in the field of R2R perovskite solar cells, specifically focusing on the compatibility of hole-transporting materials (HTLs) with the R2R coating process in terms of toxicity, scalability, stability, and costs in the context of carbon electrode-based cells. This research is pivotal for understanding the integration challenges and

potential of HTLs in scalable and practical solar cell applications. Despite the extensive body of research on perovskite solar cells, there is a notable scarcity of studies concentrating on perovskite solar cells' R2R production. Our work addresses this gap, providing key insights into the challenges of scaling up and bridging the divide between lab-scale experimentation and industrial-scale feasibility. Here, we have conducted an in-depth comparative analysis of four widely used HTL materials: spiro-MeOTAD, PEDOT, PTAA, and P3HT. Our goals are to evaluate their scalability, influence on device performance, and stability across varying humidity and temperature conditions. This work aims to deepen our understanding of the role of these HTLs on device performance in combination with a functional carbon electrode. The criteria used to select an appropriate HTL includes its ability to mitigate the poor extraction of charge by the carbon, its dissolution in an orthogonal and low-toxic non-halogenated solvent, and its additive moisture protection to the perovskite layer.

Results and discussion
Device configuration

Our previous study presented the successful implementation of R2R slot-die coating for all layers in a perovskite device, including a carbon top electrode[60]. Through that work, we uncovered the substantial influence of the PEDOT layer on modifying the perovskite/HTL/carbon interface, thereby demonstrating its significant impact on the overall device performance. Building upon these findings, the present study focuses on investigating conventional HTLs as potential R2R-friendly alternatives to PEDOT in planar NIP stacks.

Despite producing a working device, PEDOT (commercially known as HTL SOLAR3), exhibited limitations in terms of solubility in environmentally friendly solvents and scalability for cost-effective mass production. These limitations led us to search for an alternative HTL material to address these challenges and pave the way for more sustainable, and cost-effective perovskite solar cell fabrication processes.

Figure 1 illustrates the schematic of our stack, encompassing the HTL candidates: spiro-MeOTAD, PTAA, P3HT, and PEDOT which have potential for integration into the R2R coating process.

In selecting the four HTLs for our study, we strategically chose those that not only are among the most widely used in the NIP stack planar perovskite solar cells but also exhibit several key advantages that align with the objectives of high-performance and scalable solar cell production. These materials have consistently demonstrated the highest reported device performances, underscoring their effectiveness in enhancing the efficiency of perovskite solar cells[61]. Additionally, their selection was influenced by practical considerations: these HTLs are known for their ease of coating, a critical factor for ensuring uniform thin films essential for optimal device operation[62–65]. Moreover, their compatibility with R2R coating processes was a decisive factor, as it enables scalable and cost-effective manufacturing of solar panels. Our focus on these materials is intended to provide deeper insights into their potential for commercial-scale applications, addressing both performance and manufacturability aspects critical for the transition from laboratory research to industrial production.

Also, other criteria for HTL selection in this study was based on energy band alignment and prior demonstration in slot-die coating. The band energy alignment comparison between these four HTLs is also shown separately in Supplementary Fig. 1.

The energy level diagrams depicted in the schematic demonstrate the excellent compatibility of all four materials with their bottom and top layers, indicating their suitability for coating between the perovskite and carbon layers. Moreover, the solvents used for dissolving these materials are compatible with the perovskite layer, underscoring their potential for utilization in slot-die coating techniques. Nonetheless, this comparative study has yielded contrasting outcomes when attempting to scale up the process. Several factors, such as operational considerations related to slot-die coating, compatibility with carbon ink, photovoltaic performance, device stability, cost, and toxicity of the selected solvents, have displayed noticeable variations among these HTL materials.
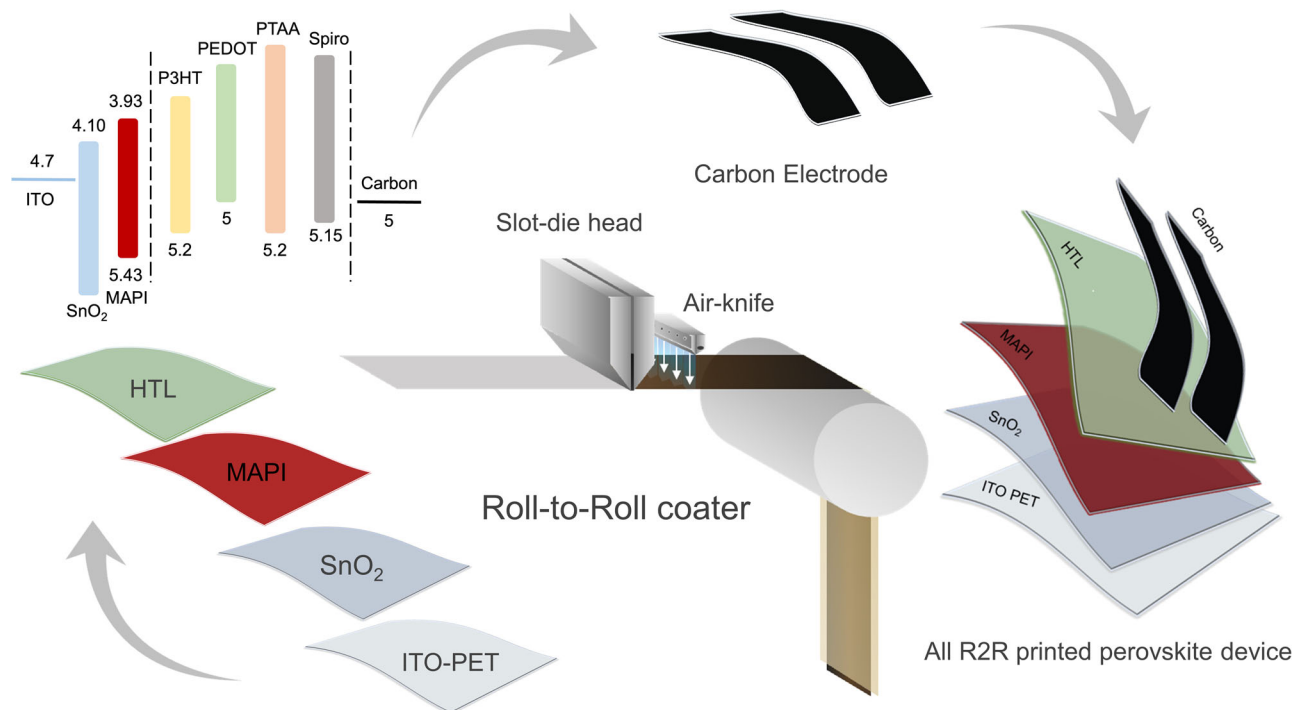
Fig. 1 | Schematic of R2R-coated perovskite solar cells with carbon electrode. The figure illustrates the design of NIP stack [tin oxide (SnO_2)/ perovskite (MAPI)/HTL/ Carbon] perovskite solar cells with various hole-transporting material candidates, including spiro-MeOTAD, PTAA, P3HT, and PEDOT.

Notably, we employed 2-methylanisole as the solvent in our carbon ink on top of these four HTLs. 2-Methylanisole stands as the green solvent choice for carbon inks due to its unique ability to yield a homogeneous and well-dispersed ink mixture, essential for uniform layer coatings in the R2R process. The choice of 2-methylanisole was necessitated by the fact that, up to the present, it was the sole viable option available within the scope of our knowledge that could be effectively utilized in a fully R2R coating of PSCs with carbon electrodes. Consequently, this study places particular emphasis on assessing the compatibility of the HTL choices with 2-methylanisole, given its pivotal role as the preferred solvent.

In the subsequent sections, an extensive analysis of each of these four layers has been conducted individually.

Spiro-MeOTAD

Among the various HTLs in the perovskite NIP stack, Spiro-MeOTAD, particularly when combined with dopants such as LiTFSI, 4-tert-butylpyridine (tBP), and FK209, has emerged as the most used. This preference stems from its exceptional charge transfer properties and its ability to facilitate the formation of uniform and compact HTL layers through easy film formation. However, the results depicted in Fig. 2 reveal that despite its prevalence in spin-coated devices with gold electrodes, Spiro-MeOTAD exhibits notably poor performance in PSCs with carbon top electrodes, resulting in significantly low device efficiency.

Both devices were fabricated using the same method for depositing all the layers except for the top electrode. Considering the high conductivity (sheet resistance: $5 \, \Omega \, sq^{-1}$) of our compact and uniform carbon electrode, we began to question the compatibility of the carbon ink with spiro and whether the drying process of the carbon layer alters the chemical structure of the layer composition. Either of these scenarios could result in a weak HTL between the perovskite and top electrode (Fig. 2a).

This discrepancy can be attributed to reduced charge transfer or increased charge recombination from the perovskite to the carbon electrode in the spiro/carbon setup, whereas the spiro/gold configuration demonstrates significantly higher current density leads to higher PV performance. Figure 2b EQE results also confirm the concept. Devices with a gold top electrode exhibit much higher current density and EQE, indicating lower

recombination and improved charge extraction. Further supporting this idea are the additional characterizations we conducted, particularly XPS results (Supplementary Fig. 2 and Supplementary Table 1) of the Spiro layer before and after solvent washing. The XPS maps revealed significant compositional changes in the Spiro layer post-washing, including the removal of additives (Li, F, Co from LiTFSI and FK209) and alterations in the elemental composition, with decreases in nitrogen and oxygen and an increase in carbon. Moreover, the observed increase in surface concentrations of lead and iodide post-washing, while indicative of some layer removal, was not substantial enough to suggest complete elimination of the Spiro layer. Rather, these findings point towards decomposition or structural alteration of the Spiro layer, leading to a loss of its hole-transporting properties. The similarity of the JV curves and plot box PCE results of devices with and without the spiro layer further supports the notion that the spiro layer is partially removed and chemically altered upon coating with the carbon layer, as depicted in Fig. 2c. Furthermore, actual photos of perovskite/spiro samples also demonstrate noticeable changes. Heating the layer slightly changes the color of spiro, due to composition changes (XPS Supplementary Table 1), while washing it with carbon ink solvent (2-methylanisole) completely removes the layer, as shown in Fig. 2d.

PTAA

PTAA stands out as a highly promising interlayer owing to its advantageous hole-transporting properties and remarkable thermal stability, making it a compelling candidate. To assess its potential, we conducted a performance analysis and compatibility evaluation of PTAA (in *O*-xylene) in our carbon electrode-based PSCs. As part of the compatibility assessment, we prepared glass/perovskite/PTAA samples and subsequently treated them with our carbon ink solvent, 2-methylanisole. Figure 3a clearly demonstrates a noticeable alteration in the quenching ability of the layer. To gain further insights, we also conducted XPS mappings for similar samples before and after washing by 2-methylanisole (Fig. 3b, Supplementary Fig. 2, and Supplementary Table 2).

To determine the coverage of the PTAA on the perovskite layer, two elements, iodide and lead, were examined on the surface. From Fig. 3b, prior to washing, it is apparent that the sample effectively covers the underlying
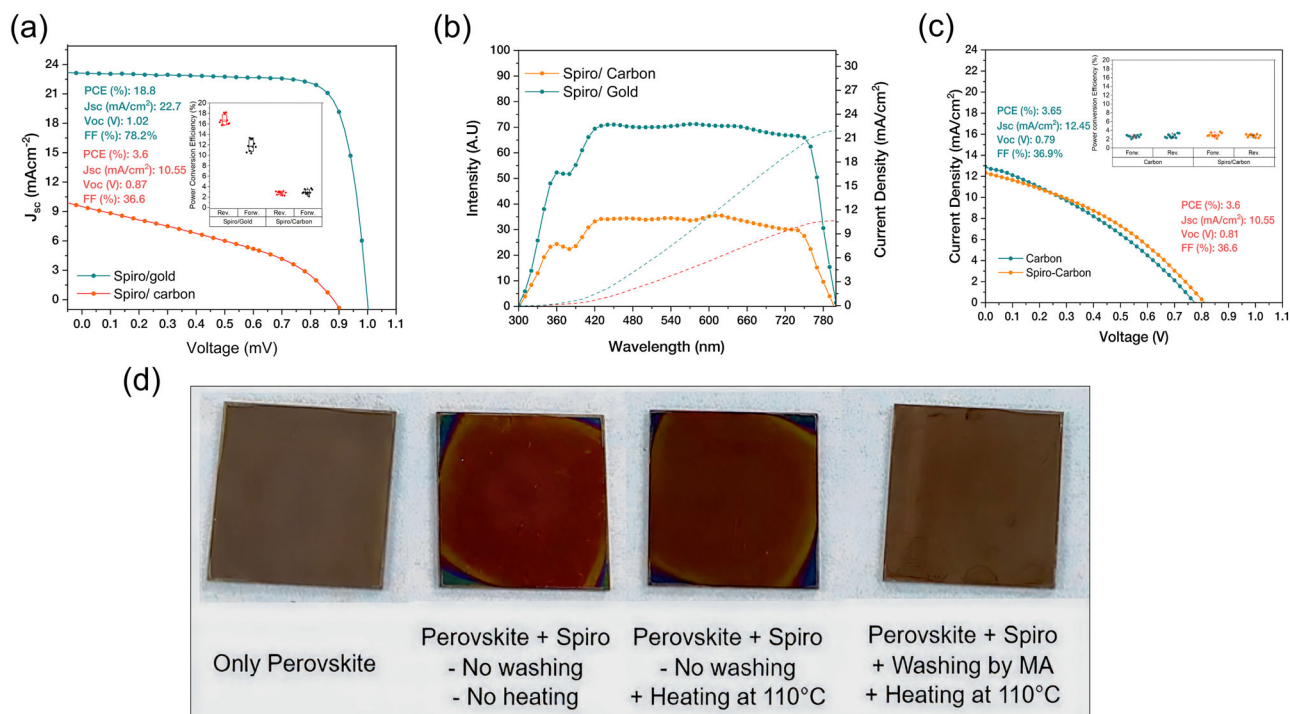
Fig. 2 | Characterization of perovskite solar cells with spiro-MeOTAD as the HTL. a, **b** J–V, plot box and EQE curves of MAPI/spiro/ gold and MAPI/spiro/ carbon samples, **c** J–V curve of perovskite/carbon and perovskite/spiro/carbon devices (with statistical results), **d** top-view photos of spiro coated perovskite samples before and after heating at 110 °C or washing by 2-methylanisole solvent.
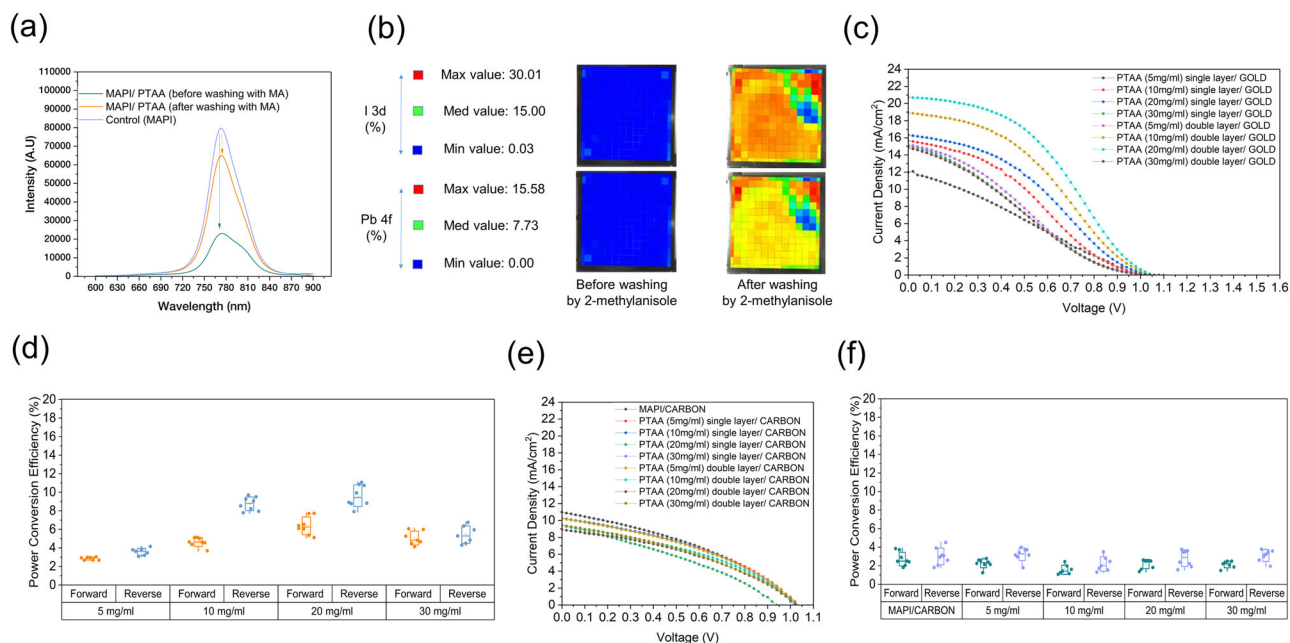

Fig. 3 | Characterization of perovskite solar cells with PTAA as the HTL behind carbon top electrode. a, **b** Steady-state PL spectra and XPS spectra mapping (for I and Pb) of MAPI/ PTAA samples before and after washing by 2-methylanisole and, **c**–**f** JV curves and statistical distribution of PCE of PSCs with different concentrations (thicknesses) of PTAA as the HTL with gold (**c**, **d**) and carbon (**e**, **f**) top electrodes.

perovskite layer, providing complete coverage. The XPS map obtained after washing the sample with the solvent serves as corroborating evidence (signs of iodide and lead on the surface), supporting the hypothesis that the carbon ink is partially removing the PTAA underneath. In conjunction with these results, we compared the photovoltaic performance of carbon electrode devices to that of gold electrode devices. JV curves and PCE plot box results of Fig. 3c, d clearly show that PTAA/gold devices displayed an improvement in efficiency as PTAA concentration (thickness) increased. To achieve greater thicknesses, we also produced PSCs with double-coated PTAA layers, and the curves reveal that higher concentrations of PTAA with double coatings resulted in higher current density (Fig. 3c, d). In contrast, Fig. 3e, f show PTAA/carbon devices exhibited consistently low efficiency without changes across all concentrations. We also observed that all the gold electrode devices displayed s-shape curves, confirming the earlier findings of
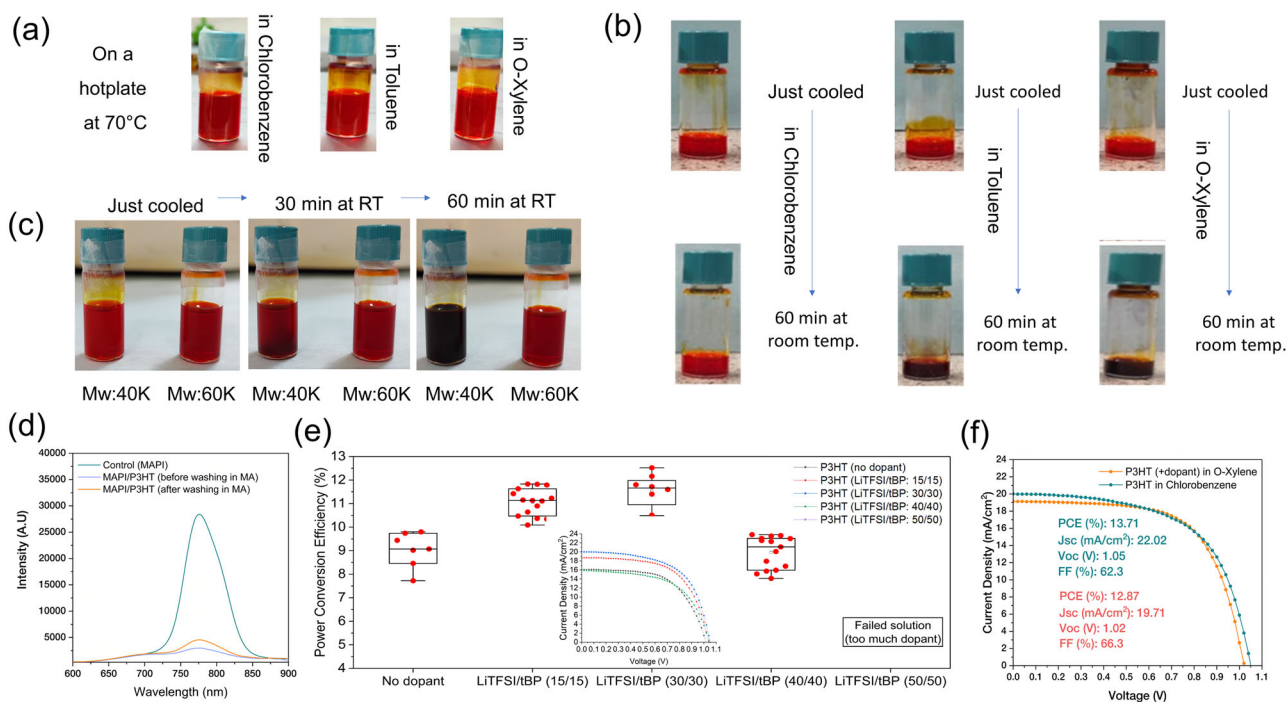
Fig. 4 | Characterization of perovskite solar cells with P3HT as the HTL behind carbon top electrode. P3HT solutions in Chlorobenzene, toluene, and *O*-xylene **a** on a hotplate at 70 °C, **b** cooled down to room temperature (RT), **c** low and high molecular weight P3HT in *O*-xylene aged at RT in a 60 min period of time, **d** steady-state PL spectra of MAPI/P3HT before and after washing by 2-methylanisole, **e** statistical distribution of PCE of PSCs with dopant engineered P3HT, and **f** J–V curves of MAPI/ P3HT/ Carbon devices with P3HT solution in chlorobenzene and in O-xylene.

weak PL quenching prior to solvent washing. Even though the PTAA/ gold devices were operational (optimized PCE ~12%), they may not be the best-performing choice for an HTL unless additional optimizations are carried out. In the case of PTAA/ carbon electrode PSCs, similar PV performance, regardless of layer thickness or solution concentration along with the results of PL and XPS, strongly suggests that PTAA and 2-methylanisole are incompatible.

P3HT

After delving into the drawbacks and compatibility challenges linked to spiro and PTAA as HTLs coated with 2-methylanisole-based carbon, our focus shifted towards another promising hole-transporting material known to be insoluble in 2-methylanisole: P3HT. P3HT has garnered widespread recognition due to its remarkable attributes as a conductive, stable, and economical HTL in PSCs. It is worth noting that P3HT exhibits high solubility in highly toxic solvents- chlorobenzene and chloroform, both of which have workplace exposure limits due to their potential health hazards. The usage of chlorobenzene is constrained due to its low Workplace Exposure Limit (WEL), which is set at ACGIH 8-hour time-weighted average (TWA) limit of 10ppm. Chloroform also has the same ACGIH 8-h TWA limit of 10ppm, making both unsuitable for scaling up coating systems. Consequently, its application is limited to small volumes to ensure compliance with safe usage limits. Alternatively, handling larger quantities of chlorobenzene would necessitate implementing rigorous and costly containment and monitoring measures. Moreover, the environmental impact stemming from the use of chlorinated solvents poses additional concerns when considering large-scale usage. Thus, our initial focus was to use alternative solvents with low toxicity, aiming for complete dissolution of P3HT.

To address this challenge, we considered comparing the solubility of P3HT in low (*O*-Xylene), medium (toluene), and highly (chlorobenzene) toxic solvents. The first two solvents, compared to chlorobenzene and chloroform, offer higher WEL ACGIH TWA values of 50 ppm (for toluene) and 100 ppm (for O-xylene), signifying lower toxicity levels. As a result, they provide safer options for handling and working within an open workspace environment typical of roll-to-roll. Supplementary Table 3 provides an overview of the toxicity hazards associated with chlorobenzene, toluene, and *O*-xylene.

To determine the optimal solubility within our potential low-toxic solvent system, we examined varying concentrations of P3HT in these solvents. Our observations indicated that when placed on a hotplate at 70 °C (Fig. 4a), all three solvents, exhibited a strong ability to dissolve P3HT. However, the behavior of P3HT in toluene and *O*-xylene differed from that in chlorobenzene when cooled down to room temperature. These solutions underwent a rapid transition from a clear, orange-colored liquid to a dark, gel-like phase. (see Fig. 4b).

It also appears that P3HT with a higher molecular weight exhibits a reduced inclination to transform from a coil-shaped into a rod-shaped polymer, as well as a diminished propensity to transition from a rod-shaped polymer to a gel-like state (crystallization)[66]. Figure 4c demonstrates that the P3HT with molecular weight (MW) 50–70 K, in comparison to the P3HT with MW 30–60 K, is less prone to undergoing gelation. To prolong the durability and delay the gelation process of the P3HT solution in O-xylene, for spin-coated PSCs, we utilized sonication for 10 minutes prior to application. This postponed the gelation process and enhanced the solution's longevity.

In contrast to the PL quenching observed for spiro and PTAA, the PL spectra for the P3HT layer before and after washing by 2-methylanisole, exhibits excellent quenching, indicating efficient charge transfer and highlights its high compatibility with this carbon ink (Fig. 4d). To evaluate the performance of P3HT HTL in our spin-coated devices, we conducted optimizations on the P3HT concentration and its dopants, LiTFSI and tBP. Figure 4e presents the J–V curves and box plot results for the optimized P3HT concentration of 20 mg ml^{-1} in O-xylene, with varying amounts of dopants (LiTFSI:tBP 1:1). The plot box in Fig. 4e reveals that the upper limit for the concentration of dopants in our P3HT solution is observed to be 40 μL. Beyond this concentration, the layer's quality is severely compromised, resulting in a complete lack of PV performance in the corresponding

device. The results validate that adding 30 µL of LiTFSI:tBP in a 1 ml P3HT solution, with a ratio of 1:1, yields the highest PCE.

Furthermore, Fig. 4f shows a comparison of the performance between P3HT layers coated with solutions in O-xylene and chlorobenzene. The highest achieved PCE for P3HT in O-xylene is 12.87%, while for chlorobenzene it is 13.71%. This disparity can be attributed to the superior dissolution capability of P3HT in chlorobenzene compared to O-xylene, which leads to differences in carrier dynamics. However, the results also indicate that O-xylene can serve as a promising low-toxic alternative solvent to the highly toxic chlorobenzene. It is important to reiterate that while chlorobenzene has been employed for slot-die coating of P3HT layers (under fume hood), its utilization presents challenges in an open workspace when transitioning to an R2R process due to exposure limits. Considering PV performance along with the toxicity concerns, it appears that O-xylene is a promising alternative solvent for dissolving P3HT and coating over a larger area.

PEDOT

Lastly, with regards to the PEDOT HTL, as mentioned earlier, our previous study showcased its exceptional performance as an interlayer between perovskite and carbon. Although this work, here, does not focus on further optimizations of PEDOT, we refer to the findings of our prior study to enhance the discussion[60].

Overview of the four HTLs performance

In the following section, we transition from the individual analysis of each of the four HTLs to a comparative examination of their respective characteristics. Herein, we discuss further why both P3HT and PEDOT demonstrate compatibility with our fully R2R manufacturing approach for device fabrication.

From Fig. 5a, roughness comparison of spiro, PTAA, P3HT, and PEDOT layers before and after washing for solvent compatibility testing revealed that initially, the spiro layer boasted the smoothest surface (RMS:

2.45 nm, mean: 9.03 nm) among the four HTLs. However, its roughness significantly increased post-washing (RMS: 11.26 nm, mean: 36.9 nm), converging towards the range observed for the perovskite layer (RMS: 14.5 nm, mean: 38.33 nm). Similarly, PTAA also exhibited increased roughness after washing (RMS: 10.42 nm, mean: 41.9 nm) compared to its pre-wash state (RMS: 5.31 nm, mean: 23.4 nm). In contrast, both P3HT and PEDOT displayed minimal changes in roughness before and after solvent washing, indicating another proof of their compatibility with the solvent. These findings underscore the importance of accounting for solvent compatibility when selecting hole transport materials for perovskite solar cells to enhance device performance and stability.

The steady-state PL and TRPL results of MAPI/spiro, MAPI/PTAA, MAPI/PEDOT, and MAPI/P3HT samples for solvent compatibility also show both P3HT and PEDOT have similar trend before and after washing. Also, the results of PL and TRPL show slightly greater quenching and shorter decay times in the P3HT sample compared to PEDOT (refer to Fig. 5b, d). Based on these results and along with the PCEs of the relevant devices (Fig. 5c), we can deduce that the increased quenching and reduced decay time observed in P3HT are attributable to a higher rate of charge recombination associated with layer defect.

Figure 5c presents a statistical PV performance of the devices using the investigated HTLs (also see Supplementary Figs. 3–6). Upon comparing devices without HTLs, it becomes evident that there is no noticeable improvement in those utilizing spiro and PTAA, as expected. In contrast, devices incorporating P3HT and PEDOT exhibit significant enhancements in efficiency. As previously mentioned, the low performance of the devices using spiro and PTAA is attributed to their partial removal by 2-methylanisole during the carbon electrode coating process. On the other hand, the enhanced PV performance observed in devices employing P3HT and PEDOT indicates not only their compatibility with 2-methylanisole but also their high charge-selecting ability, underscoring their potential for successful integration in the R2R configuration. While devices with PEDOT (HTL SOLAR3) exhibit a slightly higher PCE% than P3HT, the advantage of
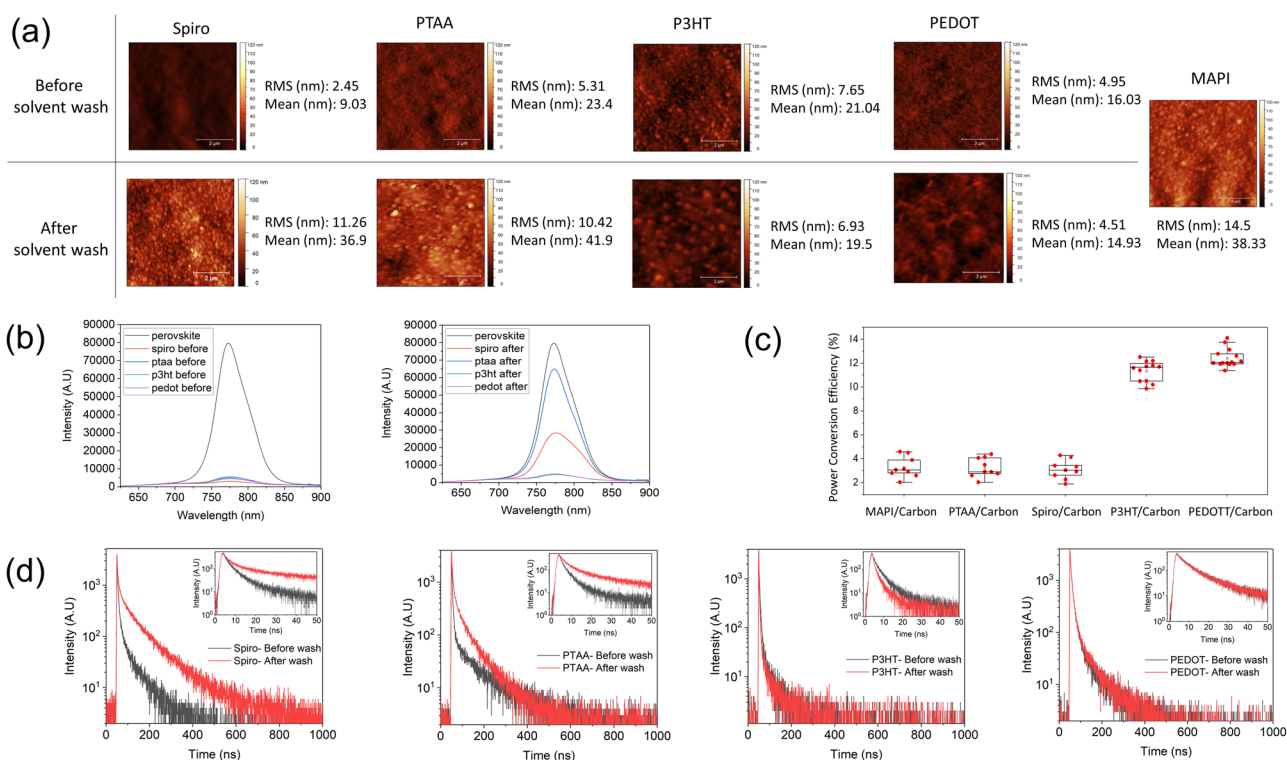

Fig. 5 | Performance overview of four various HTLS: spiro-MeOTAD, PTAA, P3HT and PEDOT. a AFM of MAPI sample as control and four HTLs coated on top of MAPI before and after washing by 2-methylanisole, **b** Steady-state PL, **c** PCE Statistical distribution, and **d** TRPL spectra of samples with spiro, PTAA, P3HT, and PEDOT HTLs.

P3HT lies in its solubility in less toxic solvent (O-xylene), rendering it a more favorable choice for R2R coating systems.

Figure 6a, b show the ISOS D3 dark (65 °C, 85%RH) and ISOS D1 dark (at 25 °C, 70%RH) stability test results for unencapsulated devices, providing valuable insights into the role of PEDOT and P3HT carbon layers in enhancing stability.

When tested under the D3 condition (at 65 °C and 85% RH), devices incorporating PEDOT demonstrated slightly better stability compared to those using P3HT. After 250 min, the devices with PEDOT retained 70% of its initial PCE, whereas the P3HT-based cell preserved 60%. In comparison to conventional spiro/gold devices, both the PEDOT/carbon and P3HT/ carbon devices exhibit remarkable humidity and temperature stability.

The D1 stability measurement results demonstrate that the devices with P3HT as the layer exhibits superior long-term stability, retaining over 85% of its initial PCE after 90 days. The devices using PEDOT also demonstrate considerable stability, maintaining over 75% of its initial PCE.

This high stability is attributed to the inherent hydrophobic properties of PEDOT, P3HT, and carbon creating a barrier that effectively repels moisture from infiltrating the perovskite layer and causing high degradation.

Cross-section images (Fig. 6c, d) of SnO_2/MAPI/P3HT/ Carbon and SnO_2/MAPI/PEDOT/Carbon reveal that both HTLs establish a favorable interface with the perovskite and carbon layers. The cross-sectional images also provide insight into the thickness of each layer. The mean thickness measurements are as follows: SnO_2 is 41 ± 7 nm, MAPI is 460 ± 31 nm, P3HT is 138 ± 33 nm, and PEDOT is 136 ± 44 nm.

R2R slot-die-coated devices

Building upon the promising results obtained from lab-scale devices employing P3HT/carbon and PEDOT/carbon, the next step was to fabricate the slot-die R2R-coated devices. Detailed information regarding the coating process of the layers can be found in the experimental section.

As previously stated, the P3HT solution in O-xylene (as a non-halogenated low-toxic solvent), tends to form a gel-like phase after being kept at room temperature for approximately 1 hour. While this is not a significant concern when employing the spin-coating method, it poses challenges during slot-die coating. The solution tends to agglomerate within the syringe tube before passing through the slot-die head, resulting in an uneven layer with agglomerated particles present on the surface. Figure 7a shows the photos of the P3HT solution (20 mg ml^{-1}, spin-coated optimized concentration) with agglomerated particles inside the wall of the tubes.

To mitigate this issue, we assessed lower concentrations of P3HT in O-xylene from 20 to 1 mg ml^{-1}. Figure 7b compares the durability of the P3HT solutions with different concentrations (20, 15, 10, 5, and 1 mg ml^{-1}) in O-xylene and chlorobenzene. Based on the photograph of the vials kept at room temperature for 24 h, concentrations below 10 mg ml^{-1} of P3HT in O-xylene showed no signs of gelation.

Figure 7c lends additional support to the idea that P3HT, when dissolved in O-xylene at concentrations below 10 mg ml^{-1}, does not aggregate along the tube walls.

Figure 7d shows the results of the spin-coated devices with different concentrations of P3HT. By decreasing the concentration from 20 to 1 mg ml^{-1}, the PCE was slightly decreased due to its lower thicknesses. Regarding the transition from spincoating to slot-die, both 5 and 1 mg ml^{-1} P3HT solutions in O-xylene were nicely coated with the slot-die coating method in sheet-to-sheet and roll-to-roll machines. Finally, to evaluate the performance of the R2R-printed device with PEDOT and P3HT HTLs, the substrates were manually diced into smaller segments, similar in size to our spin-coated devices. Randomly selected samples were then measured using conventional methods. From the JV curves of Fig. 7e, the R2R-printed perovskite devices using PEDOT exhibited the highest PCE of 10.6%. On the other hand, the devices using P3HT demonstrated a slightly lower PCE of 9.8%. The results show very close efficiencies for both PEDOT and P3HT, making them equally excellent choices for HTL in R2R PSC device fabrication. While our devices demonstrate equivalent PV performance with both PEDOT and P3HT, choosing P3HT is more advantageous due to its superior humidity stability and the use of less toxic solvents in its solution. It is worth highlighting that, along with the low-toxic solvent o-xylene in our P3HT solution, all the other layers in our N-I-P stack devices have also employed green or low-toxic solvents: DI water for SnO_2, acetonitrile as a
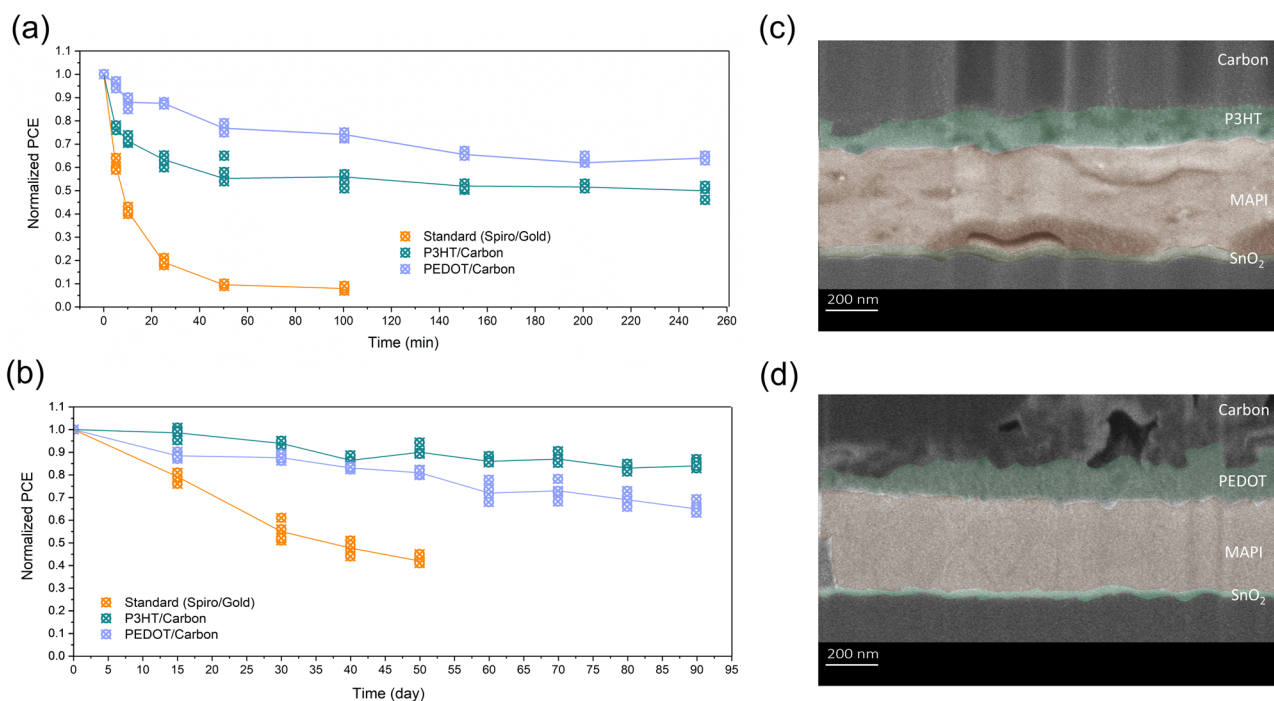
Fig. 6 | Dark stability test and cross-sectional SEM images of full NIP stack PSC devices. a Thermal/humidity stability test under 85% H at 65 °C and **b** Humidity stability test under 70% H at room temperature for P3HT/ carbon, PEDOT/ carbon, and spiro/ gold PSCs, **c** False color cross-sectional SEM images of full stack nip carbon electrode PSCs with P3HT and **d** PEDOT (scale bar 200 nm).
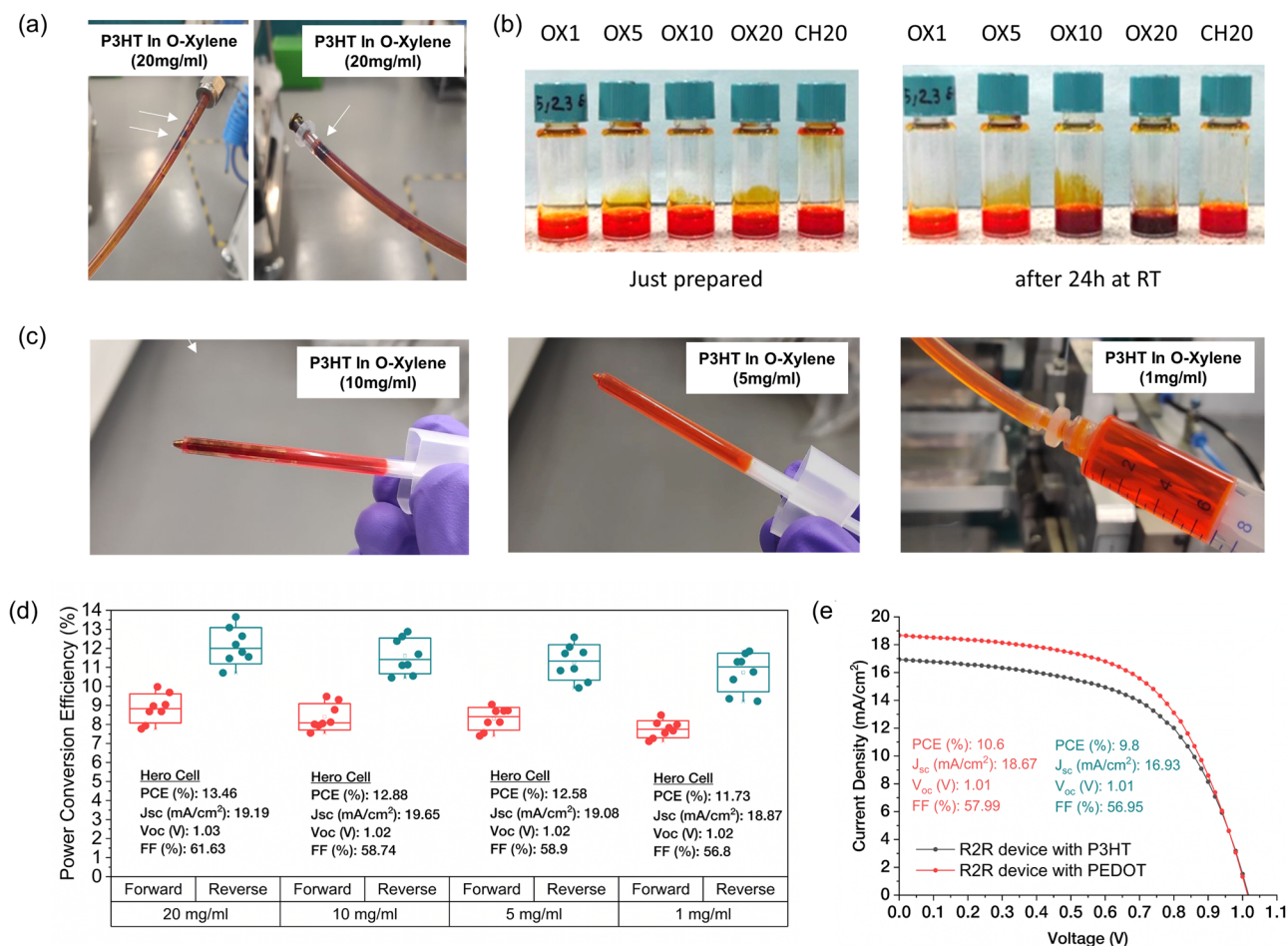
Fig. 7 | Optimization of P3HT ink concentration for slot-die R2R coating and corresponding photovoltaic performance in R2R fabricated devices. a Photos of P3HT (20 mg ml^{-1}) in O-xylene agglomeration inside the slot-die syringe tubes, **b** assessing the different concentrations of P3HT in O-xylene (OX1-20) compared to chlorobenzene (CH20) after 24 h at room temperature, **c** P3HT solution with different concentrations (10, 5, and 1 mg ml^{-1} in O-xylene) inside a tube, **d** statistical distribution PCE of spin-coated PSCs with different concentrations of P3HT and **e**) PV performance of R2R-coated PSCs with PEDOT and P3HT HTLs.

substitute for highly toxic DMF/DMSO in MAPI, and 2-methylanisole for the carbon ink, renders our devices as low-toxicity R2R-coated PSCs.

Conclusion

This study highlights the crucial significance of selecting an appropriate hole transport material in determining the photovoltaic performance and stability of perovskite solar cells utilizing carbon electrodes for R2R applications. We conducted a comparative analysis of four commonly used HTL materials: Spiro-MeOTAD, PTAA, PEDOT, and P3HT. The results emphasize that the choice of HTL material significantly influences the performance of PSCs employing carbon electrodes. We extended our investigation from rigid ITO glass substrates to fully R2R coating of PET ITO flexible substrates with a resistivity of ~50 Ω sq^{-1}. The R2R devices with HTL PEDOT achieved a PCE of 10.6%, while those with P3HT attained a PCE of 9.8%. Additionally, stability tests conducted under varying conditions (D1 and D3) demonstrated that unencapsulated PSCs incorporating carbon electrodes and these two HTL materials exhibited remarkable long-term stability. The unencapsulated devices incorporating P3HT and PEDOT demonstrated a remaining PCE of 85 and 75% after 90 days, respectively, offering improved stability when P3HT was employed. While both PEDOT and P3HT are compatible with 2-methylanisole as the carbon ink solvent in fully R2R PSCs, selecting P3HT over PEDOT is more favorable due to its higher humidity stability, use of a less toxic solvent, and lower cost. Our findings offer valuable insights for optimizing PSC performance in scalable production through R2R slot-die printing. This advancement could potentially enable the cost-effective and high-throughput fabrication of PSCs, making them suitable for emerging applications such as building-integrated photovoltaics.

Methods

Materials

All chemicals and solvents, including tin (iv) oxide colloidal dispersion liquid (Alfa Aesar, 15% in H$_2$O), P3HT (RMI-001EE, Rieke Metals), P3HT (4002-EE, Rieke Metals), Poly(TriArylAmine)-PTAA (1-Material Inc), spiro-MeOTAD powder (HPLC, 99%, Sigma-Aldrich), PEDOT (HTL SOLAR3, Ossila), carbon black and graphite (Imerys), 1-butanol (Scientific Laboratory Supplies, 99.8% anhydrous), methylamine solution (Fisher Scientific, 33% in ethanol), 2-Methylanisole (Alfa Aesar, >99%), O-xylene (Thermo Scientific Chemicals, 99%), F4TCNQ (M351 Ossila, >99%), lead iodide (PbI$_2$, TCI chemicals, 99.99%), methylammonium iodide (MAI, greatcell solar, >99% anhydrous), were purchased and used as received, without any further purification. Other chemicals and solvents, including Lithium bis(trifluoromethylsulfonyl)imide salt (LiTFSI, 99.99%), 4-tert-butylpyridine (tBP, 96%), FK209 Co(iii) TFSI salt, ethyl cellulose, acetonitrile (99.8% anhydrous), and chlorobenzene (99.8% Anhydrous) were all purchased from Sigma-Aldrich.

Spin-coat devices fabrication

The ITO glass substrates (sheet resistance:15 Ω sq^{-1}) underwent a cleaning process using an ultrasonic bath cleaner involved the use of Hellmanex solution (2%v in DI water), followed by a series of cleaning steps using DI water, acetone, and isopropyl alcohol (IPA), each step lasting 10 min. Once

the cleaning process was complete, the substrates were dried using N_2 blowing and then treated with a UV-Ozone cleaner for 15 min. This treatment was aimed at improving their wetting ability and eliminating any remaining contaminants on the surface of the substrates. To fabricate the nip stack devices, first, the ETL was formed by spincoating a diluted solution (4.2%wt SnO_2) of Tin (IV) oxide colloidal dispersion (15% in H_2O) at 4000 rpm for 30 s, then annealing at 150 °C for 10 min. The MAPI solution (0.73 M in acetonitrile) was spin-coated onto a tin oxide layer at 3000 rpm for 60 s, followed by annealing at 115 °C for 10 min. To prepare each HTL material, the following solutions were made as the optimized recipe: *P3HT:* the solution was made by dissolving 20 mg ml^{-1} of P3HT (in O-xylene) along with 15 µl (per 1 ml solution) of LiTFSI and tBT. The resulting solution was stored at 60 °C overnight. *PTAA:* A solution of 10 mg ml^{-1} of PTAA (in Toluene) was prepared and left to store at 60 °C overnight. *Spiro-MeOTAD:* A solution of 90 mg ml^{-1} (in Chlorobenzene) was prepared, and then 20, 30, and 10 µl of LiTFSI (520 mg ml^{-1} in ACN), 4-tert-butylpyridine (tBT) and FK209 (300 mg ml^{-1} in ACN) were added (per 1 ml solution) as its dopants. *PEDOT:* the HTL SOLAR3 solution was used as purchased without any further dilutions nor filtrations. All HTL solutions were coated with the same spin-coating recipe, by spinning at 3000 rpm for 40 s and annealing at 110 °C for 10 min. Finally, carbon ink was coated using a stencil and then dried at 110 °C for 10 min. The preparation details of carbon ink in 2-Methylanisole can be found in our previous work[60].

Roll-to-roll devices fabrication

The Coatema smartcoater was used to coat the tin oxide solution onto a 50 Ω sq^{-1} ITO substrate at a constant speed of 1 m min^{-1}, using a roll-to-roll slot-die coating process. No further cleaning or corona treatment was employed. The solution was diluted to 1.2%wt with DI water and 10% 1-Butanol and was printed with a wet film thickness of 7 µm (optimum), at a width of 90 mm, using a 1 mm meniscus guide and a 200 µm gap. The coated substrate was dried at 140 °C. Afterward, the 0.73 M MAPI solution was coated using the parameters of 1 mm meniscus guide, a 200 µm gap, and a wet film thickness of 7 µm (optimum) at a width of 90 mm. Following coating, an air knife with a nitrogen flow of 50 l min^{-1} was immediately used, and the coated substrate was dried at an oven setpoint of 150 °C. The PEDOT and P3HT layers were individually coated with varying wet film thicknesses of 3–6 (for PEDOT) and 2–7 (for P3HT) to determine the optimal thickness. The P3HT solution was prepared by dissolving 5 mg ml^{-1} of P3HT in O-xylene. Both HTLs were coated with a 0.25 mm meniscus guide and a 150 µm gap at a width of 90 mm. After coating, the layers were dried at 140 °C. The striped-pattern carbon electrode was coated using a method similar to our previous work[60].

Characterization

To compare the quenching ability of HTLs, the steady-state photo-luminescence spectra were acquired using the FS5 spectrofluorometer Edinburgh instrument, employing an excitation wavelength of 430 nm and a 496 nm long-pass filter in the emission pathway. Using a minibeam 6-gas cluster ion source, the XPS maps were carried out on a Kratos Axis Supra XPS instrument. The cross-section of films grown on a PET substrate was achieved in a Zeiss Crossbeam 550 FIB Field emission gun—scanning electron microscope. The Ga source FIB was operated in standard configuration with the sample surface perpendicular to the ion beam, tilted 54° to the electron beam column. A high current 30 kV 15 nA probe was used to rough trench the area, before the cross-section face was developed using lowering 30 kV probes to 30 kV 700 pA and a 55.4° tilt. The images were then recorded with an InLens secondary electron detector, and backscattered electron images were achieved with a filtered ESB detector. Atomic force microscopy (JPK NanoWizard 3) is also used to measure the roughness of the MAPI, PEDOT, and P3HT layers. 28 mm × 28 mm samples were scanned using the AFM over areas of 10 µm × 10 µm. The instrument was set to tapping mode, and samples were measured using low-stiffness Nanoworld FM50 AFM cantilevers. The scanning images were analysed using Gwyddion software (Version

2.62) to collect information on topography and determine the root mean squared (RMS) roughness.

To perform photovoltaic performance measurements on the full devices, a Keithley 2400 source meter and a solar simulator (Newport oriel Sol3A) were utilized. J–V curves were measured at 1 sun aftmouser calibration. A 5 s light soaking was applied before the potential I–V scans. All J–V curves were measured at room temperature, using a reverse scan (from 1.1 to −0.1 V) and a forward scan (from −0.1 to 1.1 V) under a constant scan speed of 85 mV s^{-1}. The active area of all devices was defined by a mask on top of the device holder, with a size of 0.09 cm². Moreover, EQE curves were obtained using a custom-built system, which consisted of Xenon arc and Quartz halogen white light sources, and a Bentham TMc300 mono-chromator. The EQE curves were measured across a wavelength range of 300–800 nm.

Data availability

The data that support the findings of this study are available in the supplementary material of this article.

References

1. Vidal, R., Alberola-Borràs, J. A., Sánchez-Pantoja, N. & Mora-Seró, I. Comparison of perovskite solar cells with other photovoltaics technologies from the point of view of life cycle assessment. *Adv. Energy Sustain. Res.* **2**, 2000088 (2021).
2. Ibn-Mohammed, T. et al. Perovskite solar cells: an integrated hybrid lifecycle assessment and review in comparison with other photovoltaic technologies. *Renew. Sustain. Energy Rev.* **80**, 1321–1344 (2017).
3. Zhang, H. et al. A universal co-solvent dilution strategy enables facile and cost-effective fabrication of perovskite photovoltaics. *Nat. Commun.* **13**, 89 (2022).
4. Holzhey, P., Prettl, M., Collavini, S., Chang, N. L. & Saliba, M. Toward commercialization with lightweight, flexible perovskite solar cells for residential photovoltaics. *Joule* **7**, 257–271 (2023).
5. Srivastava, A. et al. Lead metal halide perovskite solar cells: fabrication, advancement strategies, alternatives, and future perspectives. *Mater. Today Commun.* **35**, 105686 (2023).
6. Bati, A. S. et al. Next-generation applications for integrated perovskite solar cells. *Commun. Mater.* **4**, 2 (2023).
7. Huang, Z. et al. Wearable perovskite solar cells by aligned liquid crystal elastomers. *Nat. Commun.* **14**, 1204 (2023).
8. Ma, Y., Lu, Z., Su, X., Zou, G. & Zhao, Q. Recent progress toward commercialization of flexible perovskite solar cells: from materials and structures to mechanical stabilities. *Adv. Energy Sustain. Res.* **4**, 2200133 (2023).
9. Albrecht, S. & Rech, B. Perovskite solar cells: on top of commercial photovoltaics. *Nat. Energy* **2**, 1–2 (2017).
10. Rong, Y. et al. Challenges for commercializing perovskite solar cells. *Science* **361**, eaat8235 (2018).
11. Wang, P. et al. Solution-processable perovskite solar cells toward commercialization: progress and challenges. *Adv. Funct. Mater.* **29**, 1807661 (2019).
12. Liu, H. et al. Technical challenges and perspectives for the commercialization of solution-processable solar cells. *Adv. Mater. Technol.* **6**, 2000960 (2021).
13. Liu, X. et al. Stabilization of photoactive phases for perovskite photovoltaics. *Nat. Rev. Chem.* **7**, 462–479 (2023).
14. Ouedraogo, N. A. N. et al. Eco-friendly processing of perovskite solar cells in ambient air. *Renew. Sustain. Energy Rev.* **192**, 114161 (2024).
15. Huang, F., Li, M., Siffalovic, P., Cao, G. & Tian, J. From scalable solution fabrication of perovskite films towards commercialization of solar cells. *Energy Environ. Sci.* **12**, 518–549 (2019).

16. Vaynzof, Y. The future of perovskite photovoltaics—thermal evaporation or solution processing? *Adv. Energy Mater.* **10**, 2003073 (2020).

17. Sánchez, S., Jerónimo-Rendon, J., Saliba, M. & Hagfeldt, A. Highly efficient and rapid manufactured perovskite solar cells via flash infrared annealing. *Mater. Today* **35**, 9–15 (2020).

18. Bae, S.-R., Heo, D. & Kim, S. Recent progress of perovskite devices fabricated using thermal evaporation method: perspective and outlook. *Mater. Today Adv.* **14**, 100232 (2022).

19. Tan, L. et al. Combined vacuum evaporation and solution process for high-efficiency large-area perovskite solar cells with exceptional reproducibility. *Adv. Mater.* **35**, 2205027 (2023).

20. Kosasih, F. U., Erdenebileg, E., Mathews, N., Mhaisalkar, S. G. & Bruno, A. Thermal evaporation and hybrid deposition of perovskite solar cells and mini-modules. *Joule* **6**, 2692–2734 (2022).

21. Du, P. et al. Thermal evaporation for halide perovskite optoelectronics: fundamentals, progress, and outlook. *Adv. Opt. Mater.* **10**, 2101770 (2022).

22. Lee, J. H., Kim, B. S., Park, J., Lee, J. W. & Kim, K. Opportunities and challenges for perovskite solar cells based on vacuum thermal evaporation. *Adv. Mater. Technol.* **8**, 2200928 (2023).

23. Liu, P., Tang, G. & Yan, F. Strategies for large-scale fabrication of perovskite films for solar cells. *Sol. RRL* **6**, 2100683 (2022).

24. Bisconti, F. et al. One-step polymer assisted roll-to-roll gravure-printed perovskite solar cells without using anti-solvent bathing. *Cell Rep. Phys. Sci.* **2**, 100639 (2021).

25. Kim, Y. Y. et al. Gravure-printed flexible perovskite solar cells: toward roll-to-roll manufacturing. *Adv. Sci.* **6**, 1802094 (2019).

26. Yang, T.-Y. Roll-to-roll fabrication of perovskite solar cells using gravure printing technology. *J. Flex. Print. Electron.* **1**, 65–77 (2022).

27. Ramírez, E. A. et al. Blade-coated solar minimodules of homogeneous perovskite films achieved by an air knife design and a machine learning-based optimization. *Adv. Eng. Mater.* **25**, 2200964 (2023).

28. Gong, C. et al. Flexible planar heterojunction perovskite solar cells fabricated via sequential roll-to-roll microgravure printing and slot-die coating deposition. *Sol. RRL* **4**, 1900204 (2020).

29. Bishop, J. E., Smith, J. A. & Lidzey, D. G. Development of spray-coated perovskite solar cells. *ACS Appl. Mater. Interfaces* **12**, 48237–48245 (2020).

30. Scheideler, W. J., Rolston, N., Zhao, O., Zhang, J. & Dauskardt, R. H. Rapid aqueous spray fabrication of robust NiOx: a simple and scalable platform for efficient perovskite solar cells. *Adv. Energy Mater.* **9**, 1803600 (2019).

31. Bishop, J. E. et al. High-efficiency spray-coated perovskite solar cells utilizing vacuum-assisted solution processing. *ACS Appl. Mater. Interfaces* **10**, 39428–39434 (2018).

32. Goetz, K. P., Taylor, A. D., Hofstetter, Y. J. & Vaynzof, Y. Sustainability in perovskite solar cells. *ACS Appl. Mater. Interfaces* **13**, 1–17 (2020).

33. Gusain, A., Thankappan, A. & Thomas, S. Roll-to-roll printing of polymer and perovskite solar cells: compatible materials and processes. *J. Mater. Sci.* **55**, 13490–13542 (2020).

34. Ouyang, Z., Yang, M., Whitaker, J. B., Li, D. & van Hest, M. F. Toward scalable perovskite solar modules using blade coating and rapid thermal processing. *ACS Appl. Energy Mater.* **3**, 3714–3720 (2020).

35. Patidar, R., Burkitt, D., Hooper, K., Richards, D. & Watson, T. Slot-die coating of perovskite solar cells: An overview. *Mater. Today Commun.* **22**, 100808 (2020).

36. Zhu, P. et al. Towards the commercialization of perovskite solar modules. *Adv. Mater.* **36**, 2307357 (2024).

37. Li, Z. et al. Scalable fabrication of perovskite solar cells. *Nat. Rev. Mater.* **3**, 1–20 (2018).

38. Kim, D. H., Whitaker, J. B., Li, Z., van Hest, M. F. & Zhu, K. Outlook and challenges of perovskite solar cells toward terawatt-scale photovoltaic module technology. *Joule* **2**, 1437–1451 (2018).

39. Parvazian, E., Abdollah-zadeh, A., Dehghani, M. & Taghavinia, N. Photovoltaic performance improvement in vacuum-assisted meniscus printed triple-cation mixed-halide perovskite films by surfactant engineering. *ACS Appl. Energy Mater.* **2**, 6209–6217 (2019).

40. Velasquez, J. P. et al. Reaching highly uniform perovskite ink flow from a slot-die head toward printed solar cells. *Adv. Eng. Mater.* **25**, 2201561 (2023).

41. Yang, T.-Y., Kim, Y. Y. & Seo, J. Roll-to-roll manufacturing toward lab-to-fab-translation of perovskite solar cells. *APL Mater.* **9**, 110901 (2021).

42. Burkitt, D. et al. Roll-to-roll slot-die coated P–I–N perovskite solar cells using acetonitrile based single step perovskite solvent system. *Sustain. Energy Fuels* **4**, 3340–3351 (2020).

43. Swartwout, R. et al. Predicting low toxicity and scalable solvent systems for high-speed roll-to-roll perovskite manufacturing. *Sol. RRL* **6**, 2100567 (2022).

44. Richards, D., Burkitt, D., Patidar, R., Beynon, D. & Watson, T. Predicting a process window for the roll-to-roll deposition of solvent-engineered SnO2 in perovskite solar cells. *Mater. Adv.* **3**, 8588–8596 (2022).

45. Sutherland, L. J. et al. Vacuum-free and solvent-free deposition of electrodes for roll-to-roll fabricated perovskite solar cells. *Adv. Energy Mater.* **12**, 2202142 (2022).

46. Li, H. et al. Fully roll-to-roll processed efficient perovskite solar cells via precise control on the morphology of PbI2: CsI layer. *Nano Micro Lett.* **14**, 79 (2022).

47. Xu, Y. et al. Recent progress of electrode materials for flexible perovskite solar cells. *Nano Micro Lett.* **14**, 117 (2022).

48. Sepalage, G. A. et al. Can laminated carbon challenge gold? Toward universal, scalable, and low-cost carbon electrodes for perovskite solar cells. *Adv. Mater. Technol.* **7**, 2101148 (2022).

49. Chen, Y. et al. Efficient and stable low-cost perovskite solar cells enabled by using surface passivated carbon as the counter electrode. *J. Mater. Chem. C* **10**, 1270–1275 (2022).

50. Zhou, H. et al. Hole-conductor-free, metal-electrode-free TiO2/CH3NH3PbI3 heterojunction solar cells based on a low-temperature carbon electrode. *J. Phys. Chem. Lett.* **5**, 3241–3246 (2014).

51. Gonzalez, L. M., Ramirez, D. & Jaramillo, F. Current status and trends of carbon-based electrodes for fully solution-processed perovskite solar cells. *J. Energy Chem.* **68**, 222–246 (2022).

52. Chen, R. et al. Low-temperature sprayed carbon electrode in modular HTL-free perovskite solar cells: a comparative study on the choice of carbon sources. *J. Mater. Chem. C* **9**, 3546–3554 (2021).

53. Chen, R. et al. Rear electrode materials for perovskite solar cells. *Adv. Funct. Mater.* **32**, 2200651 (2022).

54. Chen, H. & Yang, S. Methods and strategies for achieving high-performance carbon-based perovskite solar cells without hole transport materials. *J. Mater. Chem. A* **7**, 15476–15490 (2019).

55. Chen, H. & Yang, S. Carbon-based perovskite solar cells without hole transport materials: The front runner to the market? *Adv. Mater.* **29**, 1603994 (2017).

56. Cheng, Y. et al. Antioxidant induced bulk passivation for efficient and stable hole transport layer-free carbon electrode perovskite solar cells. *Chin. Chem. Lett.* **34**, 107933 (2022).

57. Ran, H. et al. Constructing 2D passivation layer on perovskites based on 3-chlorobenzylamine enables efficient and stable perovskite solar cells. *J. Alloy. Compd.* **926**, 166891 (2022).

58. Wang, Y. et al. Defective MWCNT enabled dual interface coupling for carbon-based perovskite solar cells with efficiency exceeding 22%. *Adv. Funct. Mater.* **32**, 2204831 (2022).

59. Narendhiran, S., Kunka Ravindran, A., Rajan Thomas, I. D., Muthu, S. P. & Perumalsamy, R. Poly (vinylidene fluoride-co-hexafluoropropylene) additive in perovskite for stable performance of

carbon-based perovskite solar cells. *Int. J. Energy Lett.* **46**, 1565–1574 (2022).

60. Beynon, D. et al. All-printed roll to roll perovskite photovoltaics enabled by solution processed carbon electrode. *Adv. Mater.* **35**, 2208561 (2023).

61. Jaffri, S. B. & Ahmad, K. S. Newfangled progressions in the charge transport layers impacting the stability and efficiency of perovskite solar cells. *Rev. Inorg. Chem.* **42**, 137–159 (2022).

62. Wang, Y. et al. PTAA as efficient hole transport materials in perovskite solar cells: a review. *Sol. RRL* **6**, 2200234 (2022).

63. Lee, K.-M. et al. Facile synthesis of spiro-core-based hole-transporting material for high-performance and stable perovskite solar cells. *Chem. Eng. J.* **454**, 139926 (2023).

64. Du, T. et al. Efficient, stable, and fully printed carbon-electrode perovskite solar cells enabled by hole-transporting bilayers. *Joule* **7**, 1920–1937 (2023).

65. Choi, H. et al. A dual functional molecule for perovskite/P3HT interface to achieve stable perovskite solar cells. *J. Mater. Chem. A* **11**, 16363–16369 (2023).

66. Zhao, K. et al. A new method to improve poly (3-hexyl thiophene) (P3HT) crystalline behavior: decreasing chains entanglement to promote order− disorder transformation in solution. *Langmuir* **26**, 471–477 (2010).

Acknowledgements

Author contributions

E.P., D.B., and T.W. designed and conceptualized the project. E.P. and O.J. prepared the solutions (also B.P.), prepared the samples for all the characterizations, and fabricated the PSC devices. E.P., D.B., and R.P. were responsible for the fabrication of fully R2R-processed perovskite solar cells. J.M. conducted the XPS analysis and mapping. S.N. performed the AFM measurements. R.G.-R. and K.V.V. carried out the time-resolved photoluminescence and photoluminescence quantum yield measurements. Also helped with the manuscript revisions. P.D. acquired the SEM images. M.D. supervised R.G.-R. and K.V.V. work. T.W. supervised the project and served as the corresponding author.

Competing interests

Trystan Watson is a Guest Editor for Communications Materials and was not involved in the editorial review, or the decision to publish, this Article. The remaining authors declare no competing interests.

Additional information

Supplementary information The online version contains supplementary material available at https://doi.org/10.1038/s43246-024-00516-1.

Correspondence and requests for materials should be addressed to Trystan Watson.

Peer review information *Communications Materials* thanks the anonymous reviewers for their contribution to the peer review of this work. Primary Handling Editors: Hairen Tan & John Plummer.

Reprints and permissions information is available at http://www.nature.com/reprints

Publisher's note Springer Nature remains neutral with regard to jurisdictional claims in published maps and institutional affiliations.